First principles studies of complex oxide surfaces and interfaces

2004 J. Phys.: Condens. Matter 16 S2509

(http://iopscience.iop.org/0953-8984/16/26/025)

INSTITUTE OF PHYSICS PUBLISHING JOURNAL OF PHYSICS: CONDENSED MATTER

J. Phys.: Condens. Matter **16** (2004) S2509–S2537 PII: S0953-8984(04)63564-8

First principles studies of complex oxide surfaces and interfaces

Claudine Noguera, Fabio Finocchi and Jacek Goniakowski

Groupe de Physique des Solides, Universités Paris VI, VII, CNRS, 2 place Jussieu, 75251 Paris cedex 05, France

Received 15 May 2003, in final form 22 July 2003
Published 18 June 2004
Online at stacks.iop.org/JPhysCM/16/S2509
doi:10.1088/0953-8984/16/26/025

Abstract

Oxides enter our everyday life and exhibit an impressive variety of physical and chemical properties. The understanding of their behaviour, which is often determined by the electronic and atomic structures of their surfaces and interfaces, is a key question in many fields, such as geology, environmental chemistry, catalysis, thermal coatings, microelectronics, and bioengineering. In the last decade, first principles methods, mainly those based on the density functional theory, have been frequently applied to study complex oxide surfaces and interfaces, complementing the experimental observations. In this work, we discuss some of these contributions, with emphasis on several issues that are especially important when dealing with oxides: the local electronic structure at interfaces, and its connection with chemical reactivity; the charge redistribution and the bonding variations, in relation to screening properties; and the possibility of bridging the gap between model and real systems by taking into account the chemical environments and the effect of finite temperatures, and by performing simulations on systems of an adequate (large) size.

(Some figures in this article are in colour only in the electronic version)

1. Introduction

Insulating oxides have been recognized for a long time as important materials, due to their many applications in electronics, catalysis, environment science, as thermal barriers, etc. However, studies of their surfaces and interfaces have substantially improved only during the last five years or so, as witnessed by the progress that has been accomplished since the publication of the first two books devoted to oxide surfaces [1, 2]. By means of more refined experimental and theoretical techniques that are becoming increasingly available, a global understanding of the electronic and structural properties of oxide surfaces, as well as of their stoichiometry and their reactivity at the atomic scale, is now rapidly progressing. More specifically, it is now widely recognized that the stoichiometry in the outer layers strongly depends upon whether

annealing is performed in ultrahigh vacuum or in air during the surface preparation, whether the material has been exposed to an oxygen or humid atmosphere, etc. Nowadays, controlled and reproducible surfaces are starting to be produced, despite the existence of extremely rich phase diagrams [3, 4], or, in the case of open or polar surfaces, despite their intrinsic instability [5, 6]. In these exotic surface configurations, atoms have a much smaller coordination number than in the bulk, and thus surface sites display specific properties in adsorption or reaction processes. The spontaneous surface structuring at the nanoscale that sometimes exists may also be used to induce specific growth processes. Not only is metal deposition on oxides currently performed to produce materials for applications in spintronics or catalysis, but nowadays one also tries to synthesize ultrathin oxide films or oxide nanoparticles on various substrates [7, 8].

Oxide surfaces and interfaces involve at least three levels of complexity. First, low coordinated atoms are subjected to much weaker electrostatic (Madelung) potentials than in the bulk, which enhances their capability for receiving or donating electrons. As far as reactivity is concerned, one can indeed state that 'each atom counts' [9]. In order to predict these effects, concepts such as *local* electronegativity [2, 10], ionocovalent character of metal–oxygen bonds [11], and screening are very useful. Electronic screening, which controls the relationship between charges and potentials, is by far much less known in oxides than in metals. This is probably due to the importance of local field effects and to the variable strength of screening, consistently with the wide range of gap width that is encountered in oxides. A second complexity arises from the richness of stable or metastable configurations that oxide surfaces may display depending upon their environment. This is especially true for transition metal oxides in which cations can have several degrees of oxidation [12]. But it is also related to surface preparation conditions: the partial pressure of oxygen or water which is present during the annealing process controls the stoichiometry in the outermost atomic layers, and the degree of hydroxylation of the surfaces strongly influences their structure and properties. Finally, a detailed description of these systems often involves a large number of degrees of freedom, especially when periodic surfaces or interfaces with large unit cells result from surface instabilities or misfits at interfaces.

It is worth emphasizing how fast oxide surface simulations have improved in the last 15 years. At the end of the 1980s, mostly classical methods, based on Born-type potentials, were used. In highly ionic compounds, they gave a fair description of the atomic structure of simple planar surfaces. The first quantum simulations were semiempirical and it took some time before all theoreticians realized that self-consistent methods were essential to obtain the correct relationship between electrostatic potentials and the position of the electronic levels [2]. Later, two families of first principles methods started being applied to oxide surfaces: *ab initio* Hartree–Fock (HF) and density functional theory (DFT) [13, 14] methods, differing in the treatment of exchange and correlation effects. Actually, both turned out to be equally efficient for predicting atomic configurations, but there were large discrepancies in the descriptions of the electronic structure. The last five years have witnessed a better control of the key ingredients of the simulations: pseudopotentials (large or small core, soft or ultrasoft), basis sets (their size, plane wave versus localized), system representation (slabs or clusters, embedding methods), and exchange–correlation functionals (generalized gradient approximation (GGA) functionals, hybrid functionals, etc) [15].

The amount and the quality of results obtained by first principles methods on oxide surfaces and interfaces have made it necessary to develop interpretative tools in parallel to numerical calculations, in order to get a deeper understanding of the physics and chemistry of these systems and to be able to make predictions on unknown systems. In the following, we will discuss how first principles methods, mainly DFT based methods, can yield important information on complex systems such as those described above, with some applications taken

from our past works, and we will mention, in passing, some analytical and numerical tools which can be usefully associated with DFT methods.

The structure of the paper is the following. Sections 2–4 focus on the electronic structure: local electronic states, charge redistribution, and screening effects, respectively. In section 5, we consider the stability of oxide surfaces in contact with external reservoirs. Finally, the simulation of 'large' systems will be considered in section 6, with an emphasis on the association between first principles methods and molecular dynamics on the one hand, and effective potential methods on the other hand.

2. Local electronic states

First principles methods take into account the quantum nature of electrons to describe the atomic bonds in a solid, a cluster, or a molecule. Among them, the DFT represents a rigorous way to reduce the many-body problem to one-electron-like Kohn–Sham (KS) equations [14] in a self-consistent effective potential and to compute ground state properties, without using any input taken from experiments. This is especially valuable when there is no reference system that can be used to make guesses about the nature of electronic states or the atomic structure. We will illustrate the capabilities of DFT methods by relying on three examples. The first one reveals the complexity of the electron distribution at a metal/oxide interface. The two materials in contact have very different electronic structures: delocalized electron states on the metal side, more localized states in the valence band (VB) and conduction band (CB) of the insulator. The second example relates to the redistribution of excess electrons when neutral oxygen vacancies are produced at an ionic oxide surface. The excess electrons are trapped by the electrostatic potential produced by the surrounding cations, in the so-called F_s centres, and do not fill CB states, as might have been naively expected. This emphasizes the importance of the Madelung potential in the physics of oxide surfaces and interfaces, which is further confirmed by the nature of the electron redistribution that takes place when the vacancy diffuses on the surface or reacts with a water molecule. The third example discusses the localization of excess electrons or holes in charged stoichiometric oxide clusters, from which general arguments on the *electronegativity of an atom in a solid* can be drawn.

2.1. Interface states at Pd/MgO(100) interfaces

The physics of metal–insulator or metal–semiconductor contacts largely relies on the nature of interfacial electronic states close to the Fermi level, which drives the value of the interfacial dipole moment, and thus the band discontinuity or the Schottky barrier height (SBH) (for a review see [16]). At perfect defectless interfaces, metal induced gap states (MIGS) are produced by the matching of delocalized metal wavefunctions with exponentially decaying insulator states in the gap energy range. They are associated with a smooth density of states (DOS) [17, 18] and are similar in spirit to the exponential tails of metal wavefunctions into vacuum that appear at clean metal surfaces. Actually, when chemical bonds across the interface are formed, [16] bonding and antibonding interfacial states also exist at well defined energies (not only in the insulator band gap energy range), which contribute to the SBH.

Figure 1 (left panel) displays the local density of states (LDOS) at a Pd/MgO(100) interface, calculated under the assumption of a perfect epitaxial geometry, with a DFT based, full-potential linearized augmented plane wave method [19]. The hybridization between the O $2p_z$ and the Pd $3d_{z^2} + 4s$ orbitals induces bonding states at the bottom of the d band in the Pd LDOS, and antibonding states in the MgO band gap close to Fermi level in the O LDOS. The O $p_{x,y}$–Pd $d_{xz,yz}$ contribution can also be seen, lower in the gap. The bonding between surface

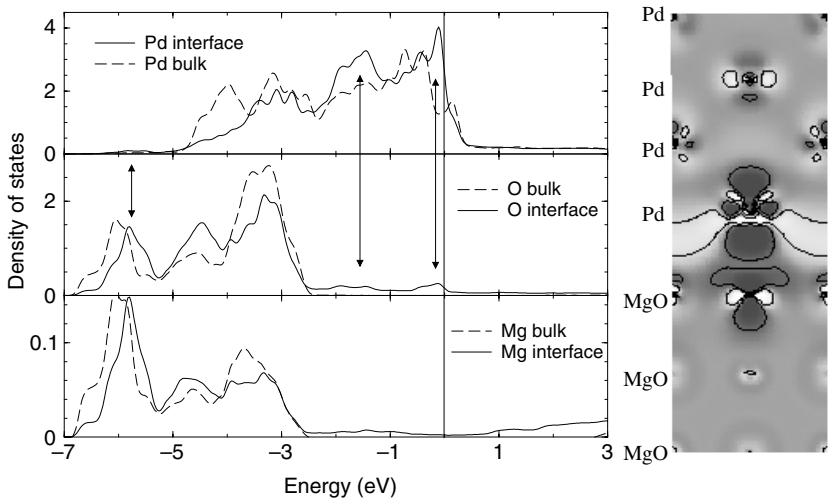

Figure 1. Left panel: the LDOS of the Pd/MgO(100) interface. Projections on both interface (full curves) and bulk (dashed curves) atoms are plotted. The LDOS is convoluted with a 0.1 eV wide Gaussian function. Right panel: differential electronic densities: $\Delta n = n_{\mathrm{Pd/MgO}} - n_{\mathrm{Pd}} - n_{\mathrm{MgO}}$. Light and dark shadings correspond to positive and negative Δn, and indicate enhanced and reduced electronic populations, respectively.

oxygen and the metal can be traced in the plots of the differential electron density Δn, figure 1 (right panel), where a clear depopulation of the O p_z and Pd d_{z^2} orbitals reflects the half-filled character of the antibonding state. The LDOS also contains signatures of conventional MIGS in the MgO band gap, at energies where no bonding or antibonding metal–oxygen states are present.

Additionally, in the interfacial metal LDOS, the VB is distorted by a crystal-field-like coupling between the spatial symmetry of the MgO electrostatic field and the spatial orientation of the metal orbitals. This polarization effect results in an electron redistribution among the different components of the metal band, which, by emptying the space above surface oxygens and by populating that above surface magnesiums, mimics the macroscopic 'image charge' effect, also clearly evidenced in the Δn plot [20, 21].

To summarize, at this interface, the DFT method helps in revealing the complexity of the electronic structure with three types of interfacial state: states due to chemical bonding which appear at well defined energies, some of which are in the MgO gap and others below the metal band; conventional MIGS associated with smooth LDOS in the MgO gap region; and LDOS distortions in the metal band due to its polarization by the electrostatic field of the ionic substrate.

2.2. Oxygen vacancies at MgO(100) surfaces

In oxide materials, defects are often present and are responsible for specific optical, transport, magnetic, or catalytic properties [1, 2, 22]. The simplest and most often encountered defects are oxygen vacancies which can exist in different charge states, depending upon the oxide and the preparation conditions. The interaction between vacancies has scarcely been investigated [23, 24], although it is a major ingredient in understanding the vacancy ordering at defective surfaces. We comment here on the nature, localization, and reactivity of the quantum state filled by the two electrons (hereafter named 'excess electrons' in reference to the already

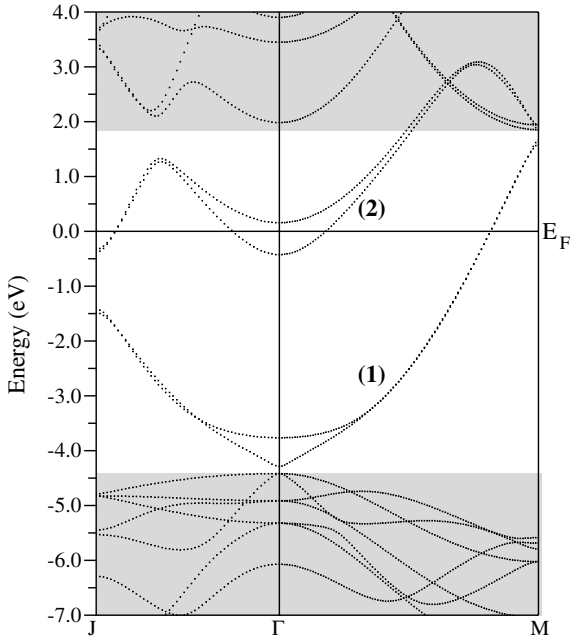

Figure 2. The band structure of the MgO(100) surface with a 100% vacancy density, plotted along the symmetry lines J–Γ–M. The two bands in the projected bulk band gap (white area) correspond to the F_s band (1) and to the surface Mg_s band (2). Degeneracy breaking around the Γ point reveals the existence of a small residual interaction between the two surfaces in the symmetric slab calculations.

filled VB of the stoichiometric oxide) left behind when a *neutral* oxygen is removed from an MgO(100) surface.

2.2.1. Localization of the excess electrons. By means of DFT total energy calculations, the electronic structure and the relaxed atomic configurations of defective MgO(100) surfaces with various neutral vacancy concentrations ($n_F = 0.125$, 0.25, 0.5, and 1) and arrangements have been determined [25]. The intuitive idea would be that the excess electrons fill empty states at the bottom of the CB. However, this is not the case at low concentration ($n_F = 12.5\%$): they are trapped in characteristic states, named F_s centres, whose energy lies in the MgO gap, $\simeq$2.2 eV above the VB maximum. Their wavefunction is highly localized at the vacancy site, as a manifestation of the strong electrostatic potential (Madelung potential) present in this highly ionic oxide. Indeed, the positively charged magnesiums which surround the vacancy create an attractive potential, able to trap electrons, in a kind of s-like 'vacancy orbital' with a radius much smaller than the Mg–O bond length.

When the vacancy density increases, these orbitals start hybridizing and forming a narrow band entirely located within the MgO surface band gap. Since the vacancy orbital bands can accommodate exactly all the excess electrons originating from the missing oxygens, they are completely filled and the surfaces are insulating. This situation occurs up to $n_F = 25\%$ and for some arrangements of vacancies at $n_F = 50\%$.

However, for other configurations with $n_F = 50\%$ and at higher concentrations, the F_s band and the surface Mg_s CB overlap (see figure 2). The vacancy states belong either to the F_s or to the Mg_s band, and their degrees of localization vary accordingly. Their partial filling

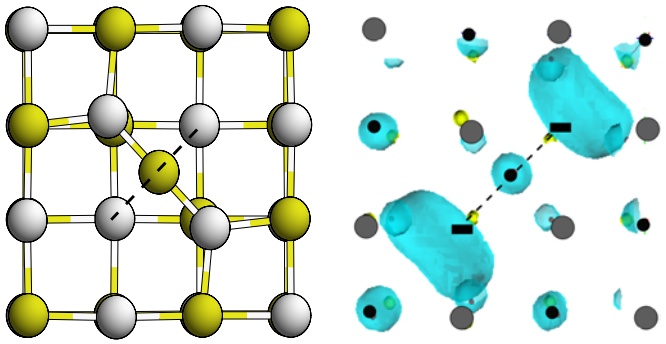

Figure 3. Characteristics of the saddle point in the diffusion path of an oxygen vacancy on MgO(100). Left panel: atomic configuration (O atoms are yellow and Mg grey). Right panel: the isodensity surface for the vacancy gap state, plotted at about 15% of the maximum state density. The diffusion path is drawn as a thick dotted line.

confers a metallic character to the surface and strongly modifies the energetics and the effective interactions between vacancies.

The diffusion of a vacancy in the MgO(100) surface layer gives rise to a complex electron redistribution and much care is needed to properly account for it [25]. Figure 3 (left panel) shows a typical diffusion path (indicated by a dashed line) between two oxygen lattice sites. The saddle point occurs when the oxygen atom lies above the top layer, at mid-distance between these sites. This configuration is characterized by a filled state, located at 2.35 eV above the top of the VB, whose electron distribution is shown in figure 3 (right panel). It presents two main lobes located at the two oxygen sites and some antibonding contribution on the diffusing atom. The empty oxygen lattice sites indeed represent the most attractive regions for the electrons (sites with the strongest Madelung potential), which are thus equally shared between them, for symmetry reasons.

It should be noted that the use of a plane wave basis to expand the eigenstates is very convenient for such a complex process, because it provides a uniform grid in real space and thus an accurate representation of the electron cloud in regions away from the nuclei. The use of localized basis sets for treating this problem, on the other hand, requires the inclusion of additional basis functions at the vacancy sites; otherwise the excess electrons could be wrongly predicted to localize on the neighbouring cations.

2.2.2. Reactivity: water dissociation. From both experimental and theoretical points of view, it is relatively well established that dissociation of an isolated water molecule on the perfect MgO(100) surface is energetically unfavourable [26–28], whether the proton and the hydroxyl group are assumed to sit at neighbouring sites or not. However, using total energy calculations and molecular dynamics simulations based on DFT, with exchange and correlation effects treated within the GGA, it has been shown [29] that a vacancy site may induce water dissociation. This process is rather involved: the dissociated state is only a local energy minimum. The global minimum corresponds to a recombined configuration, in which the oxygen initially in the water molecule adsorbs in the vacancy and the two hydrogens form a H_2 dimer. From the analysis of the corresponding energy barriers, such a final state is predicted to be quite easily reachable. This conclusion is consistent with the experimental observation that temperature-programmed desorption spectra of water taken on an Ar-bombarded MgO(100)

surface, and annealed under either O_2 or H_2O rich atmospheres practically coincide, suggesting that water is able to heal point defects (probably O vacancies) as molecular oxygen does [30].

We comment here on the electronic structure of the dissociated state (precursor of the recombination), in which the hydroxyl group is bound to two surface Mg atoms close to the vacancy and the proton sits at the vacancy site. The LDOS no longer shows evidence of the vacancy state in the gap but displays a new state at the top of the VB, well localized on the proton, which we interpret as a complex formed by the s-like F_s state with the proton. Its energy is lower than the isolated F_s level, which indicates a stabilizing electrostatic interaction between them. The neighbouring surface oxygen states shift upwards in the energy scale, because of the weakening of the surface Madelung field. The corresponding energy gain and the quite radical modification of the electronic structure accompanying the dissociation of the adsorbed water molecule are signs of the capability of the oxygen-deficient MgO(100) surface of dissociating water. Indeed, as more thoroughly discussed in section 2.4, the F_s state can be anticipated to show a more basic character than the fivefold coordinated O ions at the (100) perfect surface.

To summarize this section, the analysis of the electron redistribution around oxygen vacancies at MgO(100) surfaces stresses the domination of electrostatic over orbital hybridization effects in highly ionic oxides such as MgO. In more covalent materials, such as TiO_2, electrons are less localized and a careful account of electrostatic and covalent effects is required to obtain a reliable description of the ground state electronic structure. However, we will show in the next section that electrostatic effects are still of prime importance in small *charged* $(TiO_2)_n$ clusters.

2.3. Titanium oxide clusters

The variety of electronic properties met with in bulk titanium oxides (insulating character for TiO_2, existence of a metal–insulator transition in Ti_2O_3, and metallicity for TiO) motivates the study of titanium–oxygen based clusters and nanoparticles, which might in principle show very peculiar properties as a function of their size, composition, and atomic configuration. Their presence in cosmic dusts, due to the relative abundance of the elements Ti and O in the interstellar space [31], also raises the question of their stability.

Small unsupported clusters represent systems in which neither the atomic nor the electronic ground state configurations may be easily predicted from the knowledge of bulk properties. In particular, an open question is the extent of charge redistribution when they are either ionized or non-stoichiometric. The general answer to this question is related to the distribution of the Madelung potential in the clusters and to their screening properties [15].

We have analysed the localization of excess electrons or holes in $Ti_nO_{2n}^{\pm}$ clusters ($n = 1$–3), as obtained through geometry optimization in DFT based simulations, using the local spin density approximation (LSDA) for the exchange and correlation energy [32, 33]. Here, we focus on the most stable Ti_3O_6 isomer to exemplify the results obtained in other $(TiO_2)_n$ clusters. The Ti–O bonding in the neutral cluster has a mixed ionic and covalent character, with occupied states showing a prevalent oxygen character, and low lying empty states being largely dominated by Ti d orbitals. On the other hand, the cationic clusters $Ti_3O_6^+$ have their excess hole strongly localized on oxygens in essentially non-bonding states. A symmetric situation arises for anionic $Ti_3O_6^-$, in which the excess electron is on a non-bonding, Ti-like orbital, as shown in figure 4.

Due to its irregular shape, the Ti_3O_6 cluster possesses inequivalent Ti and O atoms. Like in other $Ti_nO_{2n}^{\pm}$ clusters obtained by the same method, it turns out that the excess hole or electron always localizes on the atom (oxygen or titanium) which experiences the weakest (in absolute

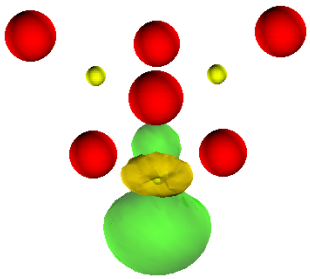

Figure 4. The excess electron state in a $Ti_3O_6^-$ cluster (Ti atoms are here drawn in yellow and oxygen atoms in red). The two green and yellow lobes of the excess state have opposite signs.

value) electrostatic potential (V_i in equation (2.3) below). In most cases, this is the atom with the smallest coordination. In addition, the excess charge induces a modification of the ground state electron density, which is truly a screening effect. It manifests itself as a weakening (and thus an elongation) of the neighbouring Ti–O bonds (see section 4).

The strength of the Madelung potential also drives the variations of the vertical electron affinities A_v as a function of the cluster geometry. This is confirmed by the fact that the sum $\epsilon_{Ti_{3s}} + A_v$, involving the 3s core level position of the Ti which experiences the weakest Madelung potential, is constant within $\simeq$10% of A_v. Thus, although the KS eigenvalues $\epsilon_{Ti_{3s}}$ are affected by systematic errors, their small *variations* have a physical meaning and reflect the change in the electronic structure of the cluster.

Before closing this subsection, it is worth mentioning that the excess charge tends to delocalize as much as possible within the LSDA. For instance, it is shared between symmetry-equivalent sites in $Ti_nO_{2n}^{\pm}$ clusters, which may lead to a 'metallic' state in an extended system. At variance with this, the HF method favours strong electron localization. This is exemplified in the study of the charged NiO(100) monolayer [34], in which the removal of symmetry constraints allows the electronic configuration to relax to non-degenerate insulating states, with an additional electron or hole fully localized on a single site. The actual degree of localization of the excess charges in insulating oxides and the capability of the various theoretical approaches for describing the actual quasi-particle states still remain topical questions.

The example chosen here shows that the value of the electrostatic potential is of fundamental importance in understanding the nature of donor or acceptor states, even in moderately covalent oxides such as TiO_2. The experience gained through the years in the theoretical investigations of oxides in low dimensionality (surfaces, interfaces, clusters, ultrathin films) can be fruitfully discussed in the framework of the concept of 'local electronegativity' for an atom *in a solid*. The next subsection describes the role played by the local Madelung potential in determining the local reactivity of an ionocovalent oxide.

2.4. Local electronegativity in insulating oxides

The electronegativity χ of an atom gives a measure of its ability to accept or donate electrons. It is thus related to the values of the ionization potential I and the electron affinity A. Mulliken proposed an electronegativity scale derived from a quantum chemical description of the isolated atom. According to his definition, χ is equal to the negative of the first derivative of the total energy E of the atom with respect to its electron number N. By using a finite difference approximation to estimate the variations in energy, one can show that the electronegativity $\chi = -I$ or $-A$ depending upon whether subtraction ($dN < 0$) or addition ($dN > 0$) of

electrons is considered. The original formulation by Mulliken can be nicely recast within the DFT, and generalized to bound systems such as molecules and solids. We recall the variational principle for the total energy functional $E[n]$, which is at the heart of the DFT [13]: $\delta(E[n] - \mu \int \mathrm{d}\boldsymbol{r}\, n(\boldsymbol{r})) = 0$. The Lagrange multiplier associated with the conservation of the electron number is evidently the chemical potential:

$$\mu = \frac{\partial E}{\partial N}. \tag{2.1}$$

The electron density can be written as $n(\boldsymbol{r}) = \sum_i f_i |\psi_i(\boldsymbol{r})|^2$, where f_i are the occupation numbers and $\psi_i(\boldsymbol{r})$ the eigenstates of the KS equation which reads

$$\left[-\frac{\hbar^2}{2m}\nabla^2 + v_\mathrm{s}(\boldsymbol{r};[n]) - e_i\right]\psi_i(\boldsymbol{r}) = 0. \tag{2.2}$$

Janak's theorem [35] tells us that the KS eigenvalues are related to the total energy by $e_i = -\partial E/\partial f_i$. Janak's theorem is thus fundamental to understanding the contribution of each KS orbital to the electronegativity. A common approximation is to focus on the so-called *frontier orbitals*: they are the highest occupied molecular orbitals and the lowest unoccupied molecular orbitals (HOMO and LUMO, respectively), which are only affected by changes in the electron number in the absence of any relaxation effect.

For surfaces and interfaces, it is no longer possible to consider a uniform variation of the electron population. It is thus worth defining *local* quantities that characterize the site-specific reactivity. Among them, the local hardness $\eta(\boldsymbol{r})$ quantifies the ability of a system to vary its chemical potential with respect to variations of the electron density at constant external potential: $\eta(\boldsymbol{r}) = [\partial\mu/\partial n(\boldsymbol{r})]_{v(\boldsymbol{r})}$. It can be shown that an approximate form for the local hardness can be given in terms of the electronic part of the electrostatic potential as

$$\eta(\boldsymbol{r}) = -\frac{1}{N}\int \mathrm{d}\boldsymbol{r}'\, \frac{n(\boldsymbol{r}')}{|\boldsymbol{r} - \boldsymbol{r}'|}.$$

When the external potential due to the nuclei varies, their contribution must be added; it yields the Madelung potential

$$V(\boldsymbol{r}) = e^2 \int \mathrm{d}\boldsymbol{r}'\, \frac{\rho(\boldsymbol{r}')}{|\boldsymbol{r} - \boldsymbol{r}'|},$$

where $\rho(\boldsymbol{r})$ is the total (electronic plus nuclear) charge density. For an extensive treatment, the reader is referred to the book by Parr and Yang [36] and to existing reviews [37]. Here, we aim to present a simpler approach that retains the essential concepts of the more rigorous DFT based formulation and can be easily dealt with in various physical contexts.

In stoichiometric charge transfer insulating oxides, the HOMO level, at the top of the VB, is usually strongly localized on the oxygens. The LUMO level, on the other hand, at the bottom of the CB has a prevalent cation character [15], as exemplified in the $Ti_3O_6^-$ clusters. As a trend, the lower the O or cation coordination numbers, the more exact such a statement is. To emphasize the importance of the local environment of the atoms, and its implications for the electronegativity, we consider the *effective* atomic orbital energies ϵ_i in the framework of the Hartree theory, as the diagonal matrix elements of the self-consistent Hamiltonian H, expanded on the atomic orbital basis set $|i\rangle$. Under simplifying assumptions, they read (atomic units are used) [2]

$$\epsilon_i = \langle i|H|i\rangle = \epsilon_i^{(0)} - U_i Q_i - V_i. \tag{2.3}$$

In equation (2.3), $\epsilon_i^{(0)}$ is the atomic orbital energy in the isolated neutral atoms i; U_i is the intra-atomic electron–electron repulsion integral, Q_i is the ionic charge, and V_i is the

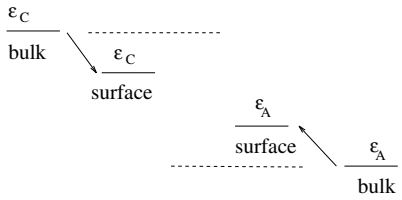

Figure 5. Shifts of the effective atomic orbital energies ϵ_i (see equation (2.3)) (i = A for an anion and i = C for a cation) when passing from bulk to surface, due to the reduction of the Madelung potential (V_i in equation (2.3)). This effect exemplifies a case of electronegativity modification at undercoordinated sites.

Madelung potential exerted on site i by the surrounding charges. In the solid, ϵ_i differs in two respects from its free-atom counterpart ϵ_i^0 (see equation (2.3)). First, the intra-atomic correction $U_i Q_i$ is related to the excess (the loss) of electron–electron repulsion on the anion (the cation) under consideration, with respect to the neutral atoms. The second correction is due to the electrostatic potential V_i. It lowers the oxygen levels and raises the cation levels, while the intra-atomic term acts in the opposite direction. The two contributions are thus in competition, and their balance is controlled by screening properties, which are globally driven by the optical dielectric constant [2].

When the HOMO or LUMO has a well defined atomic character, using equation (2.3), the Mulliken electronegativity takes the following form:

$$\chi_i = \chi_i^0 + U_i Q_i + V_i \tag{2.4}$$

which establishes that the electronegativity χ_i of the *atom in the solid* [2] is different from that of the isolated neutral atom χ_i^0 and strongly depends upon the actual atomic arrangements.

This simplified expression may be used as a guideline for understanding the *variations* of ionization potentials and electron affinities for atoms in a low coordinated environment, as well as their basicity and acidity, that is their *individual* capabilities for donating or receiving electrons, respectively. As stated above, the Madelung potential V_i acting on a surface atom or on atoms embedded in small clusters or ultrathin films strongly differs from its bulk value. Since its variations usually overcome those of the intra-atomic correction in equation (2.3), the behaviours of ϵ_i and χ_i can be discussed as a function of V_i. As schematically illustrated in figure 5, electron removal preferentially happens on the oxygen atoms experiencing the smallest Madelung potential. Similarly, electron addition starts taking place on the non-bonding cationic orbital of lowest energy, i.e. subject to the weakest Madelung potential (in absolute value), as found in the study of small $(TiO_2)_n$ clusters [32]. These concepts are useful guidelines for understanding or predicting the reactivity of nanoparticles and of specific sites at rough oxide surfaces.

3. Modifications of the ionocovalent bonding in low dimensional oxides

The detailed study of the electron distribution $n(\boldsymbol{r})$, which is the basic variable in the DFT, can also reveal the bonding characteristics of a solid compound. In insulating oxides, $n(\boldsymbol{r})$ is strongly inhomogeneous due to the difference in electronegativity between the elementary constituents. Although the charge transfers between anions and cations seem to be naturally related to the ionic character of the bond [38], a quantitative definition of the bond mixed ionocovalent character is not yet achieved. Moreover, $n(\boldsymbol{r})$ changes sensitively whenever the local environment of the atoms is modified and thus the electron distribution in small clusters, in thin films, or at surfaces can differ noticeably from its bulk counterpart. In both cases, aside

from a direct consideration of electron density maps, one needs to define integrated quantities such as the ionic charges, although they cannot be measured directly. In the following, first we recall how charges can be estimated in first principles methods, then how they can be used to define local bonding in low dimensional ionocovalent materials. Then, we illustrate these concepts on small titanium oxide clusters and on the polar MgO(111) surface.

3.1. Atomic charges

In insulating oxides, early models assigned formal charges (e.g. O^{-2}, etc) to the ions, equal to their respective valences. However, such a simplified assumption cannot be justified: as theoretical and experimental works have shown, bonds usually have a mixed covalent and ionic character, in which electron sharing coexists with charge transfer in variable proportions, which have been correlated with the asymmetric/symmetric character of the electron distribution along the bond [38]. Other models, such as that of Mulliken population analysis, start from the quantum description of the electron distribution. First principles methods provide an accurate determination of $n(r)$, which usually passes through the expansion of eigenstates $\{\psi_i\}$ and the electron density onto a basis set. Mulliken therefore considered the projection of the ψ_i on basis functions $|n, \lambda\rangle$ centred on the ions ($|\psi_i\rangle = \sum_{n,\lambda} a^i_{n,\lambda}|n, \lambda\rangle$) and took into account the overlap $S_{n\lambda,m\mu} = \langle n\lambda|m\mu\rangle$. The charge Q_n of the nth atom in the solid was then defined as the difference between its actual electron number N_n and the value N^0_n in its neutral state:

$$Q_n = N^0_n - N_n = N^0_n - 2\sum_{i=\mathrm{occ}}\sum_{\lambda}|a^i_{n,\lambda}|^2 - \sum_{i=\mathrm{occ}}\sum_{m\neq n}\sum_{\lambda,\mu}(a^i_{n,\lambda}a^{i*}_{m,\mu}S_{n\lambda,m\mu} + a^i_{m,\mu}a^{i*}_{n,\lambda}S^*_{n\lambda,m\mu}). \tag{3.1}$$

Apart from the sum over the occupied states, the cross terms $a^i_{n,\lambda}a^{i*}_{m,\mu}S_{n\lambda,m\mu}$ are assumed to be equally shared between the atoms n and m. Whether orthogonal or non-orthogonal basis functions are used, the charges depend sensitively upon the actual basis set. This is why only variations of the Mulliken charges Q_n between two systems that are represented within the same basis set are meaningful. Yet, a large degree of arbitrariness remains in their definition, which makes it impossible to compare Q_n values in different ionocovalent compounds.

A more adequate method, in relation with DFT based approaches, consists in partitioning the real space into non-overlapping volumes, in a way which is completely independent of the basis set, as first proposed by Bader [39, 40]. He noted that, although atoms lose a part of their identity in molecules or in condensed phases, these systems remain commonly considered as a collection of atoms linked by a network of bonds according to our chemical intuition. Therefore, searching for a more fundamental and rigorous definition of the *atom in a molecule*, he focused on the properties of the Schrödinger equation, which he derived from the Schwinger principle of stationary action, by introducing a Lagrangian L that is function of the fields Ψ, $\boldsymbol{\nabla}\Psi$, $\dot{\Psi}$. At the stationary point (which corresponds to the physical solution Ψ of the N-electron Schrödinger equation):

$$L^{(0)} = -\frac{\hbar^2}{4m}\sum_i \int \mathrm{d}\boldsymbol{r}_1 \cdots \int \mathrm{d}\boldsymbol{r}_N \, \nabla^2_{r_i}\Psi(\boldsymbol{r}_1, \ldots, \boldsymbol{r}_N)\Psi^*(\boldsymbol{r}_1, \ldots, \boldsymbol{r}_N) = -\frac{\hbar^2}{4m}\int \mathrm{d}\boldsymbol{r}\, \nabla^2 n(\boldsymbol{r}).$$

In an isolated atom, $L^{(0)}$ vanishes since the integration reduces to a surface integral of the type $\int \boldsymbol{\nabla}\Psi \cdot \hat{\mathbf{n}}(\boldsymbol{r})$ (where $\hat{\mathbf{n}}(\boldsymbol{r})$ is the surface normal at the point $\boldsymbol{r}$) which is null because of the natural boundary conditions. In close analogy, for a molecule or a solid, the variational principle leading to the Schrödinger equation for the global system can be derived within the additional conditions of flexible boundaries between non-overlapping domains $\Re = \bigcup_K \Re_K$, in such a way that $\int_{\Re_K} \mathrm{d}\boldsymbol{r}\, \nabla^2 n(\boldsymbol{r}) = 0$. The mathematical condition defining the partitioning of

space into atomic basins $\Re_K$ implies that no electron density flux passes through the boundary of[1] $\Re_K$ and is usually formulated as

$$\nabla n(\boldsymbol{r}) \cdot \hat{\mathbf{n}}(\boldsymbol{r}) = 0 \tag{3.2}$$

in which $\hat{\mathbf{n}}(\boldsymbol{r})$ is the normal to the boundary surface at the point $\boldsymbol{r}$. Topological atomic charges (as well as other properties, in principle) are then straightforwardly obtained from the integral of the total electronic density within each basin $\Re_K$. This analysis usually requires great care in the numerical evaluation of first and second derivatives of $n(r)$, as well as in the determination of extremal points (maxima, minima, or saddle points). In principle it can also be carried out on the electron density derived from HF or post-HF calculations. This was the case, for example, in an embedded cluster study of bulk MgO and Al_2O_3 [41], which found the two oxides to be highly ionic. Although Bader's charges cannot be directly measured, unlike dynamic (Born) charges [42], once the electron density is precisely known (even from an experimental determination [43–45]) the partition of space is uniquely defined and presents no ambiguities. The calculation of the topological charges in the framework of pseudopotential plane wave calculations in the ABINIT code has been recently implemented by our group [46].

3.2. The bond electron transfer method

Considering the local electronic structure at surfaces or in low dimensional systems, it appears that atomic charges, which are a result of the complex interplay between oxygen–cation orbital hybridization and local coordination, are much less sensitive to the local environment than the energy levels of frontier orbitals. It is thus important to clarify the relationship between these quantities. To this end, we have proposed interpreting the topological charges obtained through first principles calculations with the help of the bond electron transfer method (BETM) [11, 15], which bridges between first principles calculations and tight-binding models.

Starting from the purely ionic limit, in which oxygens and cations bear formal charges (Q^0_{O} and Q^0_{C}, respectively), we have shown that, under a few simplifying assumptions, the electron sharing due to orbital overlap can be recast as a sum of bond contributions $\Delta_{\mathrm{O}_i\mathrm{C}_j}$, consistently with the physical intuition. For simple insulating oxides with a completely filled oxygen-derived VB, the charges on an anion O_i or a cation C_j are expressed as

$$Q_{\mathrm{O}_i} = Q^0_{\mathrm{O}} + \sum_{\mathrm{C}_j} \Delta_{\mathrm{O}_i\mathrm{C}_j} \qquad Q_{\mathrm{C}_j} = Q^0_{\mathrm{C}} - \sum_{\mathrm{O}_i} \Delta_{\mathrm{O}_i\mathrm{C}_j}. \tag{3.3}$$

The summation runs over the first neighbours of each atom. Each electron transfer Δ, being related to a *bond*, concerns *two* atoms and appears in the expression for their charges. It can be shown that Δ is a monotonic function of $\beta/(\epsilon_{\mathrm{C}} - \epsilon_{\mathrm{O}})$, that is, the ratio between the resonance integral β associated with the orbital hybridization and the difference in energy between the hybridized cation and oxygen atomic orbitals involved. Δ vanishes in the ionic limit (either $\beta = 0$ or $\epsilon_{\mathrm{C}} - \epsilon_{\mathrm{O}} \to \infty$). Its magnitude thus characterizes the strength of the covalent bonding and is directly related to the local electronic properties of the two bound atoms. In general—and this is especially the case in low dimensional systems—each inequivalent bond j is associated with a distinct parameter Δ_j.

According to the BETM, the charge borne by a cation Z-fold coordinated to oxygen is equal to $Q = Q_{\mathrm{C}} - Z\Delta$ if all bonds are equivalent. In such a simple case, and under the hypothesis that the electron transfers Δ were constant independently of the chemical environment, a charge *increase* would always result from a reduction of Z. However, it is

[1] This statement must not be confused with the vanishing of the quantum mechanical current $\boldsymbol{j} = -[i\hbar/(2m)](\Psi^*\nabla\Psi - \Psi\nabla\Psi^*)$, which distinguishes the subsystem from the total isolated system in a stationary state.

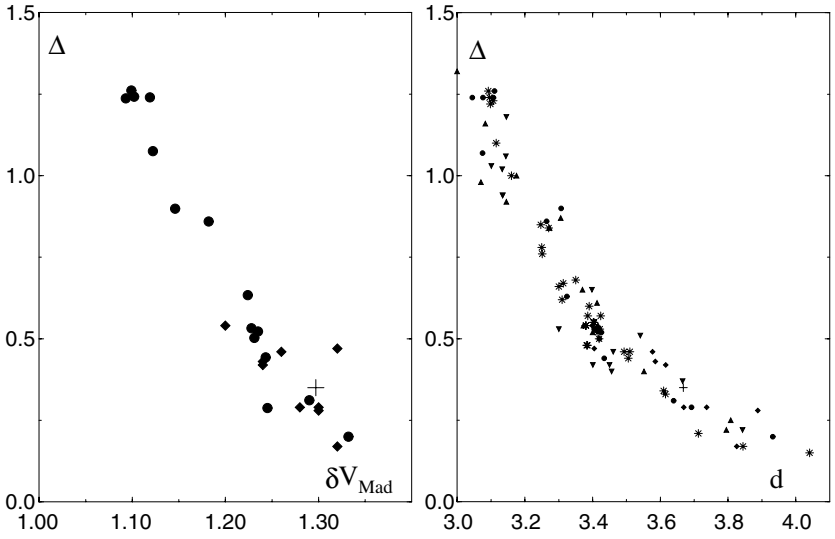

Figure 6. Left panel: electron transfer per Ti–O bond Δ as a function of the difference δV_{Mad} in the Madelung potentials acting on the Ti and O (in hartrees per electron). Right panel: the same, as a function of the calculated Ti–O bond length (in atomic units). Results for neutral stoichiometric clusters, charged clusters, bulk rutile TiO_2, and the $TiO_2(110)$ surface are represented by filled circles, stars, plus signs, and diamonds, respectively (from [32]).

precisely the influence of the local environment that is reflected in the bond electron transfers Δ, through the ratio $\beta/(\epsilon_{\mathrm{C}} - \epsilon_{\mathrm{O}})$. β varies with interatomic distances and bond angles, which can strongly differ from bulk values when low coordination atoms are considered. The effective levels ϵ_{C} and ϵ_{O}, on the other hand, are renormalized with respect to their values in the neutral atoms, as discussed in section 2.4, equation (2.2). For a given pair of bound atoms, the difference between the Madelung potential acting on cation C and O, respectively, renormalizes the difference $\epsilon_{\mathrm{C}} - \epsilon_{\mathrm{O}}$. Compact environments usually yield large Madelung potentials, which imply large differences $\epsilon_{\mathrm{C}} - \epsilon_{\mathrm{O}}$, and are thus expected to produce quite small electron transfers per bond Δ, approaching the ionic limit $\Delta = 0$. Conversely, weak Madelung potentials—which can be due to less electropositive cations or result from open structures—determine large bond electron transfers Δ, or, equivalently, small atomic charges according to equation (3.3). Therefore, the analysis of Δ provides a simple way to characterize the variable ionic and covalent contributions to the bonds in various environments. We stress that, although approximate in nature, the present application of the BETM does not rest on any empirical parameter, being based on the computed values of the atomic topological charges and the additivity of each bond contribution, as stated in equation (3.3). In the following two subsections, an illustration of the BETM model in two physical situations is done.

3.3. TiO_2 clusters

The charge distributions in neutral stoichiometric Ti_nO_{2n} clusters, the $TiO_2(110)$ surface, and bulk rutile TiO_2 [32] were studied by a DFT method, followed by a Bader analysis of the electron density. Inverting equations (3.3) subsequently allowed us to determine the electron transfers Δ_i on all inequivalent bonds.

Figure 6 gives the results as a function of the difference $\delta V^i_{\mathrm{Mad}}$ in the Madelung potentials acting on the Ti and O atoms involved in the ith bond (left panel) and as a function of the Ti–O

bond length d_i (right panel). Despite rather weak charge variations in all these systems, it is striking that, in a relatively covalent oxide such as TiO_2, Δ strongly varies with the geometry: clusters, (110) surface, bulk. The Ti–O bond in some cases has a huge degree of covalent character (for example, in the molecule TiO_2, $\Delta \approx 1.24$), while in some other cases, it is moderate (in bulk TiO_2, $\Delta \approx 0.35$). Confirming the general trend predicted by the BETM, Δ decreases as δV_{Mad} increases, i.e. as the local environment of the atoms becomes more compact.

One concern of the authors of [32] was to assess the relevance of the parameter Δ in characterizing the degree of covalency of a bond, by relating it to measurable quantities. Figure 6 (right panel) shows the correlation between Δ values and the lengths d of the corresponding bonds, in the same TiO_2 systems—92 inequivalent bonds were analysed. The trend is a rapid decrease of Δ as a function of d. In the ratio $\beta/(\epsilon_{\mathrm{C}} - \epsilon_{\mathrm{O}})$ which drives the value of Δ as explained in the previous section, both numerator and denominator decrease when bond lengths are elongated, but the variations of the resonance integrals β prevail.

The dispersion of points in figure 6 is rather small, considering the large differences among the systems that were investigated. This excellent correlation between Δ and d, whatever the morphology and the size of the system, is a strong indication that the Δ parameters, although they are not measurable quantities, are relevant in assessing the nature of the anion–cation bonding. This is especially useful for $(TiO_2)_n$ clusters which, at the same time, are highly inhomogeneous and present a mixed ionocovalent character.

As in other low dimensional systems, the electron distribution at low coordinated sites is substantially modified compared to that of the bulk. The association of DFT calculations, topological charge analysis (which is also based on first principles, since it is uniquely defined and requires no input from experiment), and analytical interpretative models can disentangle various effects: the reduction of the bond number, the shift of donor or acceptor states, the increase of covalency, etc, which all strongly affect the physical and chemical properties of undercoordinated atoms.

3.4. Polar surfaces: the MgO(111) surface

Polar surfaces represent physical systems in which the electrostatic potential distribution, and thus also the charge distribution, are of prime importance. In a slab cut along a polar orientation, a simple electrostatic argument tells us that a modification of the charge density on the outer layers of the slab is required in order to cancel out the macroscopic component of the dipole moment [47]. In the simplest case of equidistant layers bearing charge densities $\pm\sigma$, it amounts to a modification of σ on m outer layers ($|\sigma_i| \neq \sigma$ for $i \leqslant m$ and $|\sigma_i| = \sigma$ for $i > m$) obeying the relationship

$$\sum_{j=1}^{m} \sigma_j = (-1)^{m+1}\sigma/2. \tag{3.4}$$

This modification may be provided either by a strong charge modification at constant atomic density—this happens on stoichiometric surfaces through anomalous filling of surface states—or, at (roughly) constant charge, on non-stoichiometric surfaces. The term 'stoichiometric' here refers to a surface whose layers have the same composition as the bulk layers. We have analysed these two scenarios in a DFT study of the MgO(111) surface, the simplest rock-salt polar surface, which displays alternating magnesium and oxygen layers [11, 48, 49]. The stoichiometric surface involves threefold coordinated Mg atoms bound to oxygen atoms located in the underlying layers. The non-stoichiometric surface of lowest energy is the so-called octopolar reconstructed (2×2) surface, with three atoms missing in the outermost layer and one in the layer below, thus forming nanopyramids pointing in the (111) direction.

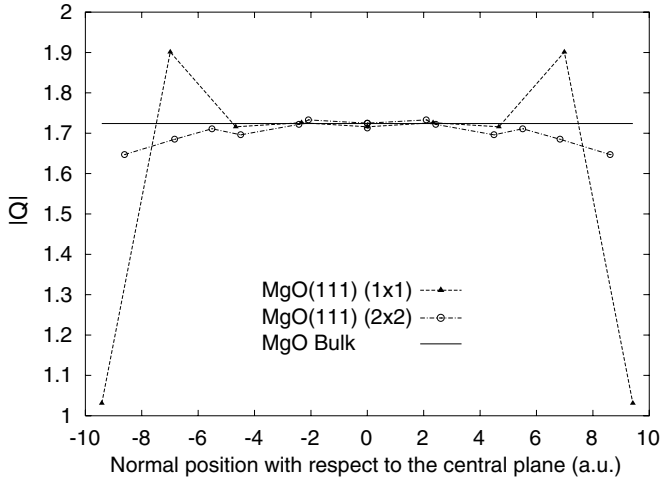

Figure 7. Absolute value of the Bader charges in MgO(111) slabs versus normal atomic positions (in atomic units) referred to the slab centre layer. Filled triangles: the stoichiometric Mg-terminated unreconstructed (1×1) surface; open circles: the non-stoichiometric (2×2) octopolar reconstructed surface; the full line shows the bulk reference.

Figure 7 shows that the charge modification on the outer layers of the stoichiometric slab is indeed very strong. On the outermost layer, the charge is nearly equal to half the bulk one, thus fulfilling the electrostatic condition (equation (3.4)). On the other hand the charge modifications on the reconstructed (2×2) octopolar surface are much weaker, and resemble those on other non-polar surfaces. Considering the atomic density in the outer layers ($1/4$ in the outermost layer and $3/4$ on the subsurface layer), the electrostatic condition is also fulfilled. Actually, no stoichiometric (111) surface has ever been observed in rock-salt oxides. It is likely that the filling of the low lying cationic surface states is unfavourable from an energetic point of view, because of the large gap. Non-stoichiometric reconstructions seem to be the most efficient mechanism for healing the polarity in these oxides.

4. Screening effects

Screening is a consequence of electron–electron interactions in solids. It takes place whenever the electronic wavefunctions are perturbed by charges or electrostatic potentials. Screening effects are usually considered as being very weak in insulating oxides, a statement corroborated by the small value of the optical dielectric function. However, they are not as well understood as in metals or semiconductors. At surfaces, perturbing potentials may be induced by the adsorption or desorption of one or more atoms or induced by the building of an interface between two systems (i.e. a metal and an oxide), or they may simply derive from the atomic-scale rearrangement of the surface, as in surface reconstructions. In general, when the physical dimensions of a system approach the characteristic length scale of screening, the latter can strongly change with respect to that of the bulk. Low dimensionality effects could be used to prepare surfaces and interfaces with new and exotic properties and their understanding constitutes a topical issue in surface science. The variety of the structural and electronic properties of oxides makes them especially interesting in this respect.

4.1. Electronic polarizability and charge redistribution

The self-consistent relation between the electron density $n(\boldsymbol{r})$ and the effective single particle potential $v_{\mathrm{s}}(\boldsymbol{r})$ is at the very heart of DFT, as well as HF theories. Accordingly, any variation

of either v_s or n is necessarily reflected in both functions. For static electric perturbations, which are *small* or *local* compared to the intrinsic properties of the unperturbed extended system, all physical quantities are modified up to first order, which is usually referred to as the *linear response theory*. For example, a change $\delta v(\boldsymbol{r})$ in the *external* potential $v(\boldsymbol{r}) \rightarrow v(\boldsymbol{r}) + \delta v(\boldsymbol{r})$ is accompanied by a first order variation of the electron density: $n(\boldsymbol{r}) \rightarrow n(\boldsymbol{r}) + \delta n(\boldsymbol{r})$, according to (with $\chi(\boldsymbol{r}, \boldsymbol{r}')$ the *polarizability*):

$$\delta n(\boldsymbol{r}) = \int \mathrm{d}\boldsymbol{r}'\, \chi(\boldsymbol{r}, \boldsymbol{r}')\delta v(\boldsymbol{r}') \tag{4.1}$$

and by a modification of the total effective potential in the KS equations $\delta v_s(\boldsymbol{r}') = \delta v(\boldsymbol{r}') + \delta v_H(\boldsymbol{r}') + \delta v_{XC}(\boldsymbol{r}')$, where both Hartree and exchange–correlation contributions ($v_H(\boldsymbol{r}')$ and $v_{XC}(\boldsymbol{r}')$, respectively) change. Within the linear response theory, equation (4.1) can be generalized to the electron density and the one particle effective potential as

$$\delta n(\boldsymbol{r}) = \int \mathrm{d}\boldsymbol{r}'\, \chi^{(0)}(\boldsymbol{r}, \boldsymbol{r}')\delta v_s(\boldsymbol{r}') \tag{4.2}$$

with $\chi^{(0)}$ the *independent particle polarizability*, whose name refers to the virtual, non-interacting system used to derive KS equations. The relation between χ and $\chi^{(0)}$ reads

$$\chi = [1 - \chi^{(0)}(\delta v_H/\delta n + \delta v_{XC}/\delta n)]^{-1}\chi^{(0)} \tag{4.3}$$

where matrix notation is used, which omits the integration over real space variables for the sake of conciseness.

Note that whenever the induced density is described in reference to an *external* potential, the full polarizability χ must be used, which, according to equations (4.1) and (4.3), is sensitive to exchange and correlation effects. It is thus clear that distinct approximations for the exchange and correlation energy functionals imply different response properties. The evaluation of $\chi^{(0)}$ usually makes use of the KS eigenvalues e_i or eigenfunctions ψ_i, according to (with $\delta^+ \rightarrow 0^+$)

$$\chi^{(0)}(\boldsymbol{r}, \boldsymbol{r}') = 2\sum_{i,j}(f_i - f_j)\frac{\psi_i(\boldsymbol{r})\psi_j^*(\boldsymbol{r})\psi_i^*(\boldsymbol{r}')\psi_j(\boldsymbol{r}')}{e_i - e_j - \mathrm{i}\delta^+} \tag{4.4}$$

where the f_i are the occupation factors of the quasi-particle states. However, it is not obvious whether wavefunctions and eigenvalues obtained from a ground state calculation, within the current approximations for the exchange–correlation energy—which is often given in the LDA or GGA forms—are a good approximation to the true quasi-particle solutions that correctly include all electron–electron interactions. As regards surfaces and interfaces, many authors have shown that LDA or GGA eigenfunctions and eigenvectors can be rather different from their quasi-particle counterparts. This happens at metal surfaces because of image effects [50], or can be due to the enhanced localization of surface or interface states as in GaAs(110) [51]. Another important case is represented by correlated transition metal oxide surfaces. It is well known that LDA or GGA poorly account for the ground state electronic structure of many bulk TM oxides, such as NiO, CoO, and MnO [52]. In particular, the hybridization of the TM d states with the O p states at the VB maximum may be very sensitive to the actual treatment of exchange and correlation effects, with important consequences for measurable properties such as magnetic moments and quasi-particle band dispersion [53]. Recently, self-interaction corrected calculations of the NiO(100) surface have appeared [54], which show that, with respect to the bulk, the exchange coupling within the surface layer is slightly reduced, whereas the coupling perpendicular to the surface is enhanced.

All contributions in equation (4.4) usually depend on $\boldsymbol{r}$ and $\boldsymbol{r}'$ separately, and not simply on $|\boldsymbol{r} - \boldsymbol{r}'|$, as in homogeneous systems. These are called *local field* (LF) effects, which reflect the inhomogeneous distribution of the electron density in space and are particularly

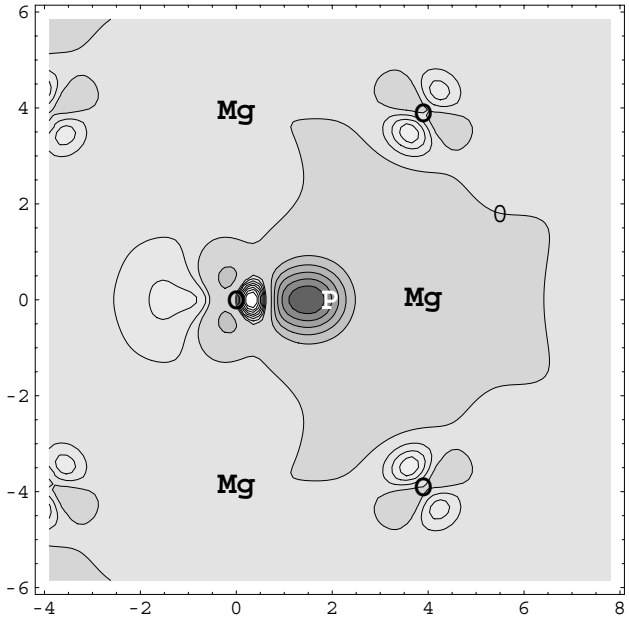

Figure 8. An isodensity map of the induced density $n_{\mathrm{ind}}^{(\mathrm{LDA})}$ in MgO in response to a Gaussian perturbation centred on an interstitial site, labelled P, in MgO. The dark and bright areas represent negative and positive values, respectively. The isodensity curves are separated by 0.0001 au^{-3}. Length scales are in au.

important in charge transfer oxides. LF effects in insulating oxides can be imaged in real space and studied by computing the density that is induced by a weak localized perturbing potential. While the actual form of the potential has a quantitative relevance, the local field effects can be qualitatively considered by relying upon a Gaussian perturbation. This has been done for several compounds in a wide range of ionicity, such as Si, $SrTiO_3$, and MgO [55]. The intensity of the on-site induced electron density is related to the magnitude of the (ground state) unperturbed electron density. On the other hand, moving some ångströms away from the centre of the perturbation, characteristic oscillations of the induced density appear, which are closely connected to the orbital structure at the band gap edges. These *medium range effects* are visible in figure 8. While approximate polarizability models, based upon the local density as the basic variable [56], are quite successful in reproducing the on-site screening, medium range effects can be reasonably accounted for only through the *ab initio* description of the matrix elements connecting the occupied and empty states, especially when localized and delocalized electronic states coexist in the CB, as in $SrTiO_3$.

As far as local effects are concerned, the gross features of static screening can be obtained by using the concept of *electron transfer per bond* described in section 3.2, in which the key factors are the energy positions of the local frontier orbitals. The *variations* of the Δ_j in response to a perturbation are used to characterize the charge redistribution $\delta n(\boldsymbol{r})$. The whole process can be schematized as follows for the case of an electron excess on a cationic site (figure 9): as a consequence of the on-site electron–electron repulsion, the cation levels move up in energy, while other levels in its vicinity are all shifted towards higher energies by the perturbing electrostatic potential. Neighbouring bonds are thus alternately more ionic ($\Delta E_n = \epsilon_{\mathrm{C}} - \epsilon_{\mathrm{O}}$ larger than ΔE in the unperturbed system) and more covalent (smaller

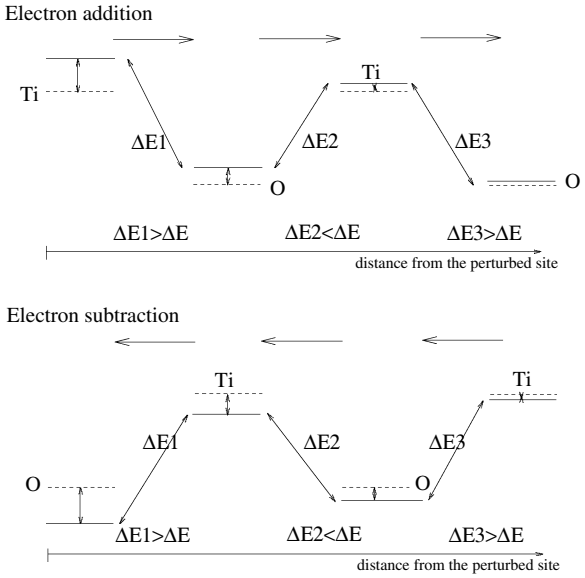

Figure 9. Modification of the positions of the effective atomic levels resulting from an electrostatic charge perturbation (dashed lines: positions in the neutral system; full line: positions in the charged system) as a function of the distance from the perturbation site (increasing n). ΔE and ΔE_n represent the difference $\epsilon_C - \epsilon_O$ in the absence and in the presence of the perturbation, respectively. Top panel: addition of an electron on a cation; lower panel: subtraction of an electron from an O. The arrows indicate the direction of the electron displacements to screen the perturbation.

$\Delta E_n = \epsilon_C - \epsilon_O$), which allows electrons to flow away from the perturbation. The spatial extent of the screening effects depends on global quantities, such as the macroscopic optical dielectric constant, as well as on local ones, such as the actual distribution of the local Madelung potential and the overlap between atomic-like orbitals.

As previously discussed in section 3.3, the electron transfers per bond Δ_i are intimately related to the bond lengths d_i. Therefore, screening processes are usually accompanied by bond length modifications. Since, according to figure 6, the more ionic the bond, the longer it is, an electron flow away from the perturbation is accompanied by alternate elongations and contractions of bond lengths. These structural effects were actually found in the simulation of TiO_2 charged clusters and surfaces. Since this scheme is pretty general, the observation of bond length variations can provide a qualitative insight into the screening mechanisms at work.

4.2. TiO_2(110) reduction upon Na adsorption

TiO_2 is known as a photocatalyst material that can be used for applications in environmental or biological science. Its (110) face is a prototype of TM oxide surfaces, since its preparation can be well controlled and, due to its semiconducting character, electronic probes, such as photoemission and scanning tunnelling microscopy, can be used for its precise characterization. Upon adsorption of electropositive alkali atoms, the surface is reduced. The localization of the donated electrons and the modifications that the electronic structure undergoes exemplify the strength of screening effects.

At low coverage, the Na valence electron is almost fully transferred to the TiO_2 substrate, as indicated by the Na topological charge which is larger than 0.9 [57]. This is consistent with the shift of Ti core levels towards lower binding energies (a signature of Ti^{3+} ions) observed by

x-ray photoemission (XPS), which was assigned to the fivefold coordinated surface titaniums (surface Ti with the smallest coordination number). Actually, DFT and Bader analysis show that this simple and rather intuitive picture is partly incorrect.

Compared to the bare surface, the additional occupied spin-polarized state is located at ≈1.8 eV above the VB maximum. Nearly no weight is found on the adsorbed Na, or on the substrate oxygens. The excess state is essentially localized on the Ti atoms *in the plane beneath the surface* with a dominant weight on those lying just below the fivefold coordinated Ti. Indeed, these Ti, although sixfold coordinated, experience a somewhat weaker Madelung potential than the surface Ti, *when the surface is fully relaxed*. On the bulk-truncated surface, the situation would be reversed.

Moreover, the total electron redistribution shows marked differences for the excess state density. This implies that strong screening effects are at work, as anticipated at the opening of this section. The excess electron, localized on the subsurface Ti, repels other electrons towards neighbouring atoms, thus affecting the total charge distribution. Another source of perturbation is provided by the Na^+ ion, which is also screened by the substrate electrons. Two screening electron fluxes thus coexist, one away from the subsurface Ti and the other directed towards the adsorbed Na, which interfere due to the proximity of the two perturbations. It is possible to understand the process by simply inspecting the variations of the Ti–O bond lengths. Around the Ti perturbation, all Ti–O bond lengths increase, indicating an electron flux away from the site, which washes out a part of the negative perturbing charge.

The final result of these concomitant screening processes questions the simple picture put forward to interpret the XPS data. As a whole, with respect to the clean surface, the variation of the subsurface Ti electron number does not exceed 0.1 electrons, while, on the bridging oxygens next to the Na adsorption site, it amounts to about 0.13 electrons. Nevertheless, the DFT result are consistent with experimental data: on the one hand, upon adsorption, the computed variations of the Ti 3s binding energy are reduced on average by ≈0.7 eV, in agreement with XPS data, although there is a non-negligible dispersion due to screening. On the other hand, the calculated VB is narrowed by ≈0.4 eV, also in agreement with experiment, as a consequence of the increase in ionicity in the TiO_2 substrate.

As coverage c increases, the nature of the screening changes considerably. The Ti levels around which the excess electrons are localized shift towards higher energy, due to the on-site electron–electron repulsion. Simultaneously, Na-like energy levels shift towards lower energy, due to the electrostatic potential created by neighbouring Na cations. A crossing between Na and Ti states can thus be foreseen for some critical coverage.

Our results show a minor variation of the Na electron number (in the Bader sense) for coverage values between $c = 1/8$ and 1/4ML, which means that, in this coverage range, the correct physical picture is that of a system still largely dominated by ionic interactions between the surface and the adsorbates. In contrast, when the coverage increases from $c = 1/4$ to 1/2 ML, the Na electron number grows significantly, and one excess state acquires some weight on the adsorbed layer. The Fermi level crosses Na states as well as Ti-derived states. This coincides with the onset of a covalent bonding within the adsorbed layer and with a drastic change of screening properties, which become more similar to those in a thin metal film.

5. Stability of a surface in contact with an external reservoir

Controlling, characterizing, or measuring the stoichiometry of surfaces or interfaces is among the most difficult tasks that physicists and chemists have to cope with when dealing with oxides. Part of the question is related to the surface preparation methods, which, requiring high temperature annealing, can induce atomic desorption, often of oxygen, from the outer

layers. Another source of complexity comes from the fact that the surfaces of many oxides are not uniquely defined by their orientations, since several terminations, with distinct chemical compositions, may be exposed. This is the case, for example, at corundum X_2O_3 (0001) surfaces, which can exhibit three terminations with either one or two cationic layers, or oxygens, in contact with vacuum, respectively. For polar surfaces, as mentioned above, the most efficient intrinsic stabilization mechanisms usually imply non-stoichiometric outer layers. The presence of contaminants such as water is also a concern in many experimental conditions.

In all cases, the properties, whether electronic, mechanical, or chemical, which determine the usefulness or performance of the oxide in the applications, are strongly influenced by the chemical nature and the structure of the surface. The knowledge of the actual chemical composition of the surface cannot be routinely achieved with the available experimental tools. Quantitative Auger measurements are scarce, grazing-incidence x-ray diffraction gives information averaged over coherence lengths of the order of hundreds to thousands of ångströms, and the chemical identification of atoms remains a challenge with near-field microscopies.

In this context, efforts have been made to extend DFT calculations, which in most cases predict zero temperature and zero pressure properties of a given set of atoms, in order to describe systems in contact with a chemical reservoir, such as surfaces in thermodynamical equilibrium with an atmosphere of variable composition. For this purpose, it is necessary to rely on thermodynamics and introduce the chemical potentials of the atomic constituents in the theory. The relative stability of surfaces with different stoichiometries can then be estimated by searching for the configuration with the lowest Gibbs free energy γ. A few illustrative examples on oxide surfaces and interfaces are provided by recent DFT studies on α-Fe_2O_3(0001) [58], Nb/α-Al_2O_3(0001) [59], RuO_2(110) [60], and ZnO(0001)–Zn [6]. In the following, we will quickly sketch the method used to calculate surface Gibbs free energies and then present recent results obtained in our group on $SrTiO_3$(110) and (100) surfaces.

5.1. Surface Gibbs free energy

The surface Gibbs free energy $\gamma(T, P)$ of an oxide of bulk composition X_mO_n can be estimated, within a slab model, as

$$\gamma(T, P) = \frac{G(T, P) - N_X\mu_X(T, p) - N_O\mu_O(T, P)}{2S} \tag{5.1}$$

with $G(T, P)$ the Gibbs energy of the slab with two surfaces of area S, at temperature T and pressure P. μ_X and μ_O are the chemical potentials (per atom) of the cations X and the oxygens, and N_X and N_O are their numbers within the supercell. The Gibbs free energy of the slab:

$$G(T, P) = E - TS + PV \tag{5.2}$$

contains the internal energy contribution E that is equal to the Gibbs free energy at zero temperature and pressure and can be straightforwardly computed in DFT. The entropy S can be estimated at low temperatures by calculating the phonon spectrum and using the quasi-harmonic approximation for the free energy. The two right-hand terms $-TS$ and PV are usually omitted because, in most cases, their order of magnitude is of a few meV Å^{-2}, i.e. much smaller than differences in internal energy between different surface configurations [60].

Since the oxide surface is in equilibrium with the underlying bulk oxide, the two chemical potentials μ_X and μ_O are related through

$$g_{X_mO_n}(T, P) = m\mu_X(T, P) + n\mu_O(T, P) \tag{5.3}$$

in which $g_{X_mO_n}(T, P)$ is the Gibbs free energy per formula unit of bulk X_mO_n in equilibrium with metal X and gaseous oxygen. It can be readily obtained by independent DFT calculations.

In that way, for each surface configuration i—specified by the actual termination, stoichiometry, and reconstruction pattern—the corresponding surface free energy γ_i can be estimated as a function of μ_O and the oxygen excess number $\Delta N_O^i = N_O - \frac{n}{m}N_X$ in the slab, with respect to the bulk stoichiometry:

$$\gamma_i(T, P) = \frac{G_i(T, P) - \frac{1}{m}N_X g_{X_mO_n}(T, P) - \Delta N_O^i \mu_O(T, P)}{2S}. \tag{5.4}$$

Within the allowed range of $\mu_O(T, P)$ values, the surface i with the smallest γ_i is thus predicted to be the most stable. In order to make a link with the actual experimental conditions, defined by temperature and pressure, the ideal gas expression for $\mu_O(T, P)$ as a function of the oxygen partial pressure P_{O_2} can be used:

$$\mu_O(T, P) = \mu_O^0 + \frac{1}{2}kT \log\left(\frac{P_{O_2}}{P^0}\right), \tag{5.5}$$

where μ_O^0 refers to the standard state at $T^0 = 298.15$ K, and $P^0 = 1$ atm.

5.2. Stability of $SrTiO_3$(110) and (100) surfaces

The extension of the previous scheme to ternary compounds has been used to predict the most efficient stabilization mechanism of polar $SrTiO_3$(110) and (111) surfaces [61, 62]. Along the (110) orientation, bulk $SrTiO_3$ displays a stacking sequence of atomic layers $\cdots O_2/SrTiO/O_2/SrTiO \cdots$. Assuming ionic charges equal to $Q_O = -2$, $Q_{Ti} = +4$ and $Q_{Sr} = +2$, these layers bear formal charges $Q = \pm 4$ per 2D unit cell. According to the criterion for polarity compensation (equation (3.4)) the surface charge density must be equal to half the bulk value, i.e., $Q_{surf} = \pm 2$. Two main classes of (1×1) terminations can thus be considered. On the one hand, stoichiometric terminations reflecting the bulk layer compositions—the (110) SrTiO and O_2 ones—for which an anomalous filling of surface states is expected. On the other hand, (110) surfaces with TiO, Sr, and O terminations are obtained from the stoichiometric surfaces by removal of one Sr, one Ti plus one O, or one O, respectively. These surface compositions can in principle provide the polarity compensation. As a reference, the cleavage (100) surface of $SrTiO_3$ is non-polar and displays two different stoichiometric terminations: the (100) TiO_2 and the (100) SrO, which are expected to be more stable than any polar face.

The surface Gibbs free energy γ_i of a termination i reads

$$\gamma_i = \frac{1}{2S}[G_{slab}^i - N_{Ti}\mu_{Ti} - N_{Sr}\mu_{Sr} - N_O\mu_O] \tag{5.6}$$

where the chemical potentials of the three species fulfil $g_{SrTiO_3} = \mu_{Sr} + \mu_{Ti} + 3\mu_O$ since the surface is in equilibrium with the bulk $SrTiO_3$. This yields

$$\gamma_i = \frac{1}{2S}[G_{slab}^i - N_{Ti}g_{SrTiO_3} - \mu_O(N_O - 3N_{Ti}) - \mu_{Sr}(N_{Sr} - N_{Ti})]. \tag{5.7}$$

Neglecting the $-TS$ and PV terms in G_{slab}^i, one can deduce the stability diagram in the allowed range for the O and Sr chemical potentials. Introducing the variation of chemical potentials $\Delta\mu_O = \mu_O - E_{O_2}^{mol}/2$ and $\Delta\mu_{Sr} = \mu_{Sr} - E_{Sr}^{bulk}$ with respect to the stable phases of O and Sr in equation (5.7), one obtains

$$\gamma_i = \frac{1}{2S}[\chi_i - \Delta\mu_O(N_O - 3N_{Ti}) - \Delta\mu_{Sr}(N_{Sr} - N_{Ti})] \tag{5.8}$$

with

$$\chi_i = \frac{1}{S}[E_{slab}^i - N_{Ti}E_{bulk} - \frac{E_{O_2}^{mol}}{2}(N_O - 3N_{Ti}) - E_{Sr}^{bulk}(N_{Sr} - N_{Ti})]. \tag{5.9}$$

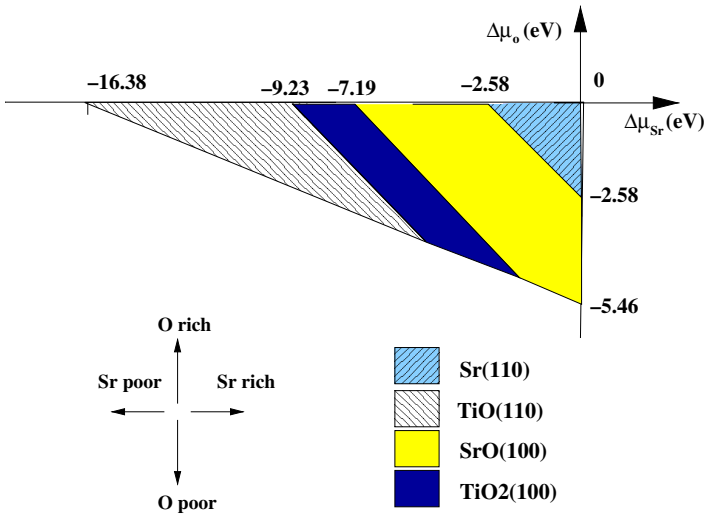

Figure 10. A stability diagram for the (1 × 1) $SrTiO_3$(110) and (100) surfaces. The most stable termination is represented as a function of the excess O and Sr chemical potentials $\Delta\mu_O$ (vertical) and $\Delta\mu_{Sr}$ (horizontal) (see the text). The triangular region in the ($\Delta\mu_O$, $\Delta\mu_{Sr}$) space represents the domain of stability of the cubic $SrTiO_3$ crystal.

Using the first principles DFT method [62], we have calculated the χ_i for stoichiometric and non-stoichiometric $SrTiO_3$(110) terminations. We find 1.73 and 4.78 J m^{-2} for the former (SrTiO and O_2, respectively) and 5.62, −1.75, and 1.27 J m^{-2} for the latter (TiO, Sr, and O, respectively). For two complementary terminations (such as TiO–Sr and SrTiO–O_2) the sum of the γ_i is independent of the chemical potentials and yields their cleavage energy.

The same theoretical and computational framework may be applied to the (1 × 1) terminations of $SrTiO_3$(100). Their surface Gibbs free energies are actually not very much lower than those of the non-stoichiometric (110) terminations, which suggests that, in particular environments, the latter can be stable. Figure 10 displays the whole phase diagram in the ($\Delta\mu_O$, $\Delta\mu_{Sr}$) plane, which corresponds to excesses of the O and Sr chemical potential with respect to O_2 (gas) and metallic Sr. In the commonest conditions, corresponding to moderate Sr and O chemical potentials, the (100) faces are favoured. However, three (110) distinct (1 × 1) terminations are also predicted to be stable.

The (110) Sr termination is the most stable in O and Sr rich environments, as its complementary (110) TiO face is in O and Sr poor conditions. From a geometrical point of view, the (110) TiO and the (110) Sr terminations can be viewed as exposing strongly relaxed {100} nanofacets. It is therefore not completely surprising that their surface energies can become comparable to those of flat {100} terraces, if the formation energy of corners and edges is not too high.

The stoichiometric and open-shell (110) SrTiO termination happens to be stable in a domain corresponding to O poor and Sr rich conditions. Although this stability domain is rather small, this is one of the very few cases of a stable stoichiometric polar oxide surface with an open-shell electronic structure. Others are RuO_2(110) [60] and ZnO(0001) [63]. However, for ZnO(0001), a recent STM investigation [6] questions the morphologies proposed in [63] and evidences different, non-stoichiometric, structural motifs. In rock-salt structures, the (1 × 1) unreconstructed (111) polar faces generally have a much higher energy than reconstructed, non-stoichiometric ones. In this respect, the peculiar behaviour of $SrTiO_3$ may be due to

the existence of several oxidation states for Ti atoms and to the presence of Ti–O covalent bonds, in conjunction with a not too large fundamental gap. Indeed, the filling of surface states needed for polarity compensation may require a smaller energy if atomic relaxation and electronic screening are substantial. The analysis of the topological charges of the (110) SrTiO termination shows an important charge redistribution affecting the surface layers. Such a screening mechanism costs less energy than a drastic charge reduction on only one or two surface atoms, which is essentially the case for MgO(111) (1×1) [49].

Our theoretical findings are consistent with the experimental evidence, which shows that $SrTiO_3\{110\}$ orientations can be quite easily obtained. However, due to the scarcity of experimental investigations and the observed complexity of the physical and chemical behaviours of the $SrTiO_3(110)$ surface, the detailed determination of its atomic and electronic structure still remains an open question. First principles calculations suggest that, even for the unreconstructed (1×1) surfaces, several terminations can be produced, depending upon the precise experimental conditions. The great dispersion of the experimental results could be due to such a sensitivity.

6. Simulations of large systems

Due to an improved efficiency of recent DFT method implementations and to progress in computer performances, the complexity of the systems which can be treated by the first principles simulations constantly increases, thus reducing the gap between what is modelled and what is of actual interest. As far as the underlying physics is concerned, two qualitatively different objectives of large-size simulations can be distinguished. One straightforwardly aims at increasing the number of independent particles taken into account in the simulations in order to better account for surface or interface large-cell reconstructions, grain boundaries, etc. The other tries to account for finite temperature properties, relevant in the experiments or the applications. In the latter case, statistical averages have to be performed over many configurations (electronic, atomic, compositional, etc), which can significantly differ from the ground state, and the convergence with respect to their number often represents a computational challenge even for a system with a moderate number of atoms. Additionally, many real systems are in a constrained/local (metastable) rather than in a global thermodynamic equilibrium. This makes the choice of initial/boundary conditions especially delicate, and allows the system to explore configurations far from the global equilibrium, in a dynamic simulation at finite temperatures.

Treatment of both classes of problems requires statistical physics tools, such as molecular dynamics or Monte Carlo techniques, in order to generate configurations that, depending upon the problem, are used to minimize the potential energy, to evaluate thermodynamic averages, or to follow the trajectory of the system. With respect to the computational treatment, two strategies can be conceived.

On the one hand, the Car–Parrinello [64] pseudopotential plane wave technique, which was designed to carry out first principles molecular dynamics simulations on the fly, is particularly useful for exploring metastable configurations of insulating systems, as we will illustrate by a study of the competition between cooperative molecular adsorption and dissociation of water on MgO(100). However, a direct use of DFT within dynamic simulations remains of limited use, either because the pseudopotential method is computationally too demanding (for atoms such as transition metal atoms or oxygens, which require a high energy cut-off), or because the number of atoms/configurations that can be explicitly treated remains relatively small.

Alternative approaches consist in using the DFT method to parametrize the energetics, which is then introduced within the statistical method. These approaches range from a mere

estimation of selected configuration energies or activation barriers, to a full parametrization of effective interatomic potentials. Although this may seem close to existing semiempirical approaches, the experimental information available in many surface or interface processes is often insufficient for designing interatomic model potentials. The use of first principles methods as a source of microscopic information is then the only possibility. We will give an application of this strategy in a study of the structural characteristics of Pd clusters on MgO(100).

6.1. Molecular/dissociative adsorption of water on MgO(100)

Trying to solve the controversy existing at the end of 1990s regarding the mode of water adsorption on perfect MgO(100) surfaces, first principles DFT simulations of 1 ML of water on MgO(100) have been performed [27, 28, 65–67]. Both strategies described above have proved crucial for a correct description of the cooperative adsorption process.

6.1.1. System size: the (3×2) *reconstruction.* The ground state ($T = 0$ K) of 1 ML of water on MgO(100) consists in a (3×2) reconstruction, which involves a dimerization between the H_2O ad-molecules, as well as a dissociation, as proved by the presence of surface hydroxyl groups [27]. It has also been pointed out that the energetics underlying the collective adsorption mode is relatively subtle. The dimerization is essential for the dissociation: no dissociation is reported for an isolated water molecule, nor for a non-reconstructed monolayer [26]. However, lateral interactions between dimers in the adsorbed layer are also essential. In fact, no dissociation takes place for isolated dimers or at lower water coverage [28].

Those simulations invalidate the predictions made when considering more constrained systems (with smaller unit cells), and give an excellent example of a physical problem in which the size of the system chosen in the simulation *qualitatively* affects the character of the solution. It also exemplifies a situation where, due to the mixed character of the adsorption—partly dissociative and partly molecular—the energetics becomes relatively complex, limiting seriously the applicability of empirical or semiempirical methods.

6.1.2. Dynamic effects: finite temperature. A system composed of weakly bounded, light molecules is considerably influenced by atomic vibrations at finite temperatures. Indeed, variations of the adsorbate atomic structure and coverage as a function of temperature have been observed experimentally [68]. Key questions are thus the stability at finite temperatures of the 0 K solution, and the degree of modification of the adsorbate atomic structure.

Constant-energy molecular dynamics simulations in the microcanonical ensemble have thus been performed directly within the pseudopotential, plane wave DFT approach [69]. At $T \simeq 200$ K, a 0.65 ps run, after 0.15 ps equilibration, was enough to ensure a satisfactory convergence of the structural and energetic characteristics. These dynamic simulations emphasize two main results. First, the general conclusions on the dissociative adsorption mode of water on MgO(100) remain valid up to finite temperatures. Due to interactions between the co-adsorbates, the ML remains partially dissociated and no attempt of hydrogen back-transfer is registered in the picosecond time range. Second, the atomic structures obtained from static and dynamic calculations differ substantially. Due to atomic vibrations, the average elevation of the adsorbed water molecules above the MgO surface increases by about $\simeq$0.1 Å, resulting in a weakening of the substrate–adsorbate interaction. Several hydrogen bonds between the adsorbate and MgO are broken and new bonds between water molecules are created, associated with interatomic distance changes of the order of 0.4 Å.

These results clearly stress the importance of dynamic effects on the state of a system. Although, in this particular case, the adsorption mode remains qualitatively unaltered, the MD results invalidate the structural predictions resulting from purely static total energy calculations. More generally, in systems characterized by a competition between several distinct configurations, finite temperature effects must be taken into account before addressing the interpretation of experimental structural data on firm grounds.

6.2. Pd clusters on MgO(100)

As a model catalyst, Pd clusters supported on MgO(100) have been the subject of many detailed experimental and theoretical studies. Understanding the cluster morphology, the relation between their size and detailed atomic structure, and their interaction with the oxide substrate is a necessary step towards the control of their reactivity. If the DFT based methods have proved their usefulness for treating simple metal/oxide interfaces, the computational effort needed to model realistic and large-size systems considerably limits their field of application. In particular, it is not yet possible to use them directly for modelling the complex interfaces involving inhomogeneous relaxations, large-cell reconstructions, dislocation networks, etc, which have been experimentally observed. This drawback is particularly constraining for understanding nanocluster structures, which require an extensive search in configurational space. On the other hand, there exist no straightforward and/or reliable semiempirical methods for modelling metal/oxide interfaces, because fundamental questions such as the extent of charge redistribution and the strength and character of interfacial interactions still remain unanswered. For these reasons, several effective approaches, derived from first principles methods, have been proposed in the last few years for treating metal/MgO interactions [70–74]. In the following, we focus on the method that was applied to study Pd clusters on MgO(100) [74].

6.2.1. Generation of the effective potential for Pd–MgO(100) interaction. The approach couples a well established second moment approximation (SMA) potential for metal–metal interactions within the cluster [75] to a many-body potential energy surface representing the metal–MgO interactions, derived from model DFT calculations. The effective metal–MgO interaction takes into account the fact that sites of on-top oxygens are energetically the most favourable for Pd adsorption, while magnesium sites represent maxima, and hollow sites are saddle points in the potential energy surface computed at the DFT level [20]. In addition, the Pd–MgO interaction depends sensitively upon the Pd coverage [76]: it is strongest for isolated ad-atoms and decreases progressively as the number Z of Pd–Pd bonds grows. This effect is particularly relevant because small clusters are characterized by a large proportion of undercoordinated atoms.

The Pd/MgO interaction is assumed to be additive with respect to the number N of Pd atoms: $E^{\mathrm{Pd-MgO}} = \sum_{i=1}^{N} E(x_i, y_i, z_i, Z_i)$. It depends on their lateral position (x_i, y_i) with respect to the MgO lattice, on their elevation z_i above the MgO surface, and on the number Z_i of their nearest Pd neighbours. The function $E(x_i, y_i, z_i, Z_i)$ is determined from a set of periodic DFT calculations assuming a perfect epitaxial geometry. With each adsorption site (oxygen, magnesium, and hollow), a particular dependence of E on the height z above the surface plane is found, and for all intermediate (x, y) positions, an interpolation between these three high symmetry points is performed. In order to determine the dependence on Z of E, DFT calculations have been carried out for three coverages: isolated Pd atoms, an epitaxial monolayer, and an epitaxial bilayer [77]. They correspond to $Z = 0$, 4, and 8, respectively, and thus cover the range of coordination numbers from isolated ad-atoms to a fully constituted Pd/MgO(100) interface.

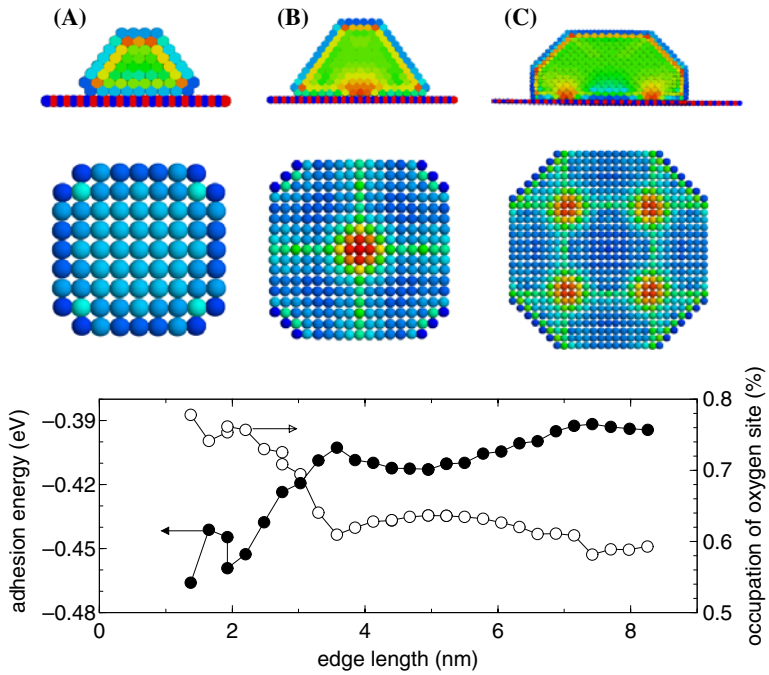

Figure 11. Pressure maps along a cut perpendicular to the substrate (top panel), and within the interfacial Pd layer (middle panel) for clusters of 2.5 (A), 4.7 (B), and 7.4 (C) nm. Dark zones correspond to a positive pressure (compression) whereas bright zones correspond to no pressure or to a negative pressure (tension). The bottom panel displays the evolution of adhesion energy (black dots) and of the average occupation of the oxygen adsorption site (open circles) as a function of cluster size (from [74]).

6.2.2. Equilibrium configurations. Clusters of different sizes (edge length) and morphologies (aspect ratio, corner truncations) were considered, under the constraint that they obey the observed [100]Pd ∥ [100]MgO epitaxy relation. For each of them, a series of quenched molecular dynamics runs, of different lengths, at various temperatures and initial conditions, has been performed (a few nanoseconds of MD runs per cluster, typically), in order to find the potential energy minimum. The main results are summarized in figure 11.

In agreement with experiments, 'flattened' pyramids with truncated edges are energetically the most stable. Due to the lattice mismatch between Pd and MgO ($a_{\mathrm{Pd}} \sim 0.92 a_{\mathrm{MgO}}$), they systematically display a tetragonal distortion, with a dilation in the interface plane, accompanied by a compression in the perpendicular direction which roughly conserves the atomic volume in the metal. Small Pd clusters (see figure 11(A)) take a quasi-pseudomorphic configuration at the interface, but, with increasing sizes, the lattice mismatch can no longer be accommodated by a mere dilation. At about 5 nm, some Pd rows start being positioned off the preferential adsorption sites (see the compression zone in figure 11(B)): an interface misfit dislocation is created, which partially releases the strain. As the size further increases, the dislocations organize themselves in a periodic network, leading to a (10 × 10) superstructure (figure 11(C)), approaching the (11 × 11) incommensurate structure observed at extended Pd/MgO(100) interfaces ($11 a_{\mathrm{MgO}} \sim 12 a_{\mathrm{Pd}}$). The bottom panel of figure 11 represents the evolution of the Pd–MgO adhesion energy as a function of cluster size. Its main contribution, due to Pd–MgO interactions, follows closely the changes in occupancy of the preferential

(oxygen) adsorption site. The energy cost related to the structural deformation of the Pd deposit is in all cases small [74].

To summarize, the use of a model interatomic potential derived from first principles calculations permits us to take into account all interfacial degrees of freedom, and to perform an extensive search of minimum-energy structures, without the constraints, such as the assumption of pseudomorphic metal/oxide structures, made in previous studies. These simulations proposed original mechanisms of strain release in the supported clusters, and gave new insight into the coupling between the nature of the interaction and the atomic structure at the interface.

7. Conclusions

The significant progress in the understanding of the physics of oxide surfaces and interfaces during the last decade is, to a large extent, due to the successful application of first principles methods and to the correlated development of tools, such as the Bader decomposition of electronic density, able to tackle oxide-specific questions.

In this paper, we have emphasized that the parallel development of fundamental concepts underlying the physics of oxides (electronegativity, charges, ionocovalency) and of first principles calculations helps in constructing and justifying general relationships between electronic and atomic structure characteristics (positions of atomic levels, atomic charges, surface termination/structure, bond lengths). We have given several examples of analytical models able to rationalize complex DFT results and to extract the basic mechanisms (modification of local electrostatic potentials, changes of bond ionocovalency) which shed light on the computed results (modification of electronic distribution, changes of bond lengths).

However, many questions concerning oxide surfaces and interfaces remain unanswered. Some of them, such as unresolved surface structures, adsorbate induced surface stability, point defects, and the properties and growth of thin oxide layers can probably be treated within the framework of existing theory. An adequate treatment of this kind of problems often requires the use of large-scale simulations in order to account for both the structural complexity and the temperature/kinetics-dependent factors.

Other unsolved questions require us to go beyond a mere description of ground state properties. Indeed, seeking an account of excitations, band gaps, and screening at oxide surfaces and interfaces remains a major field of development/application of theories and computational schemes.

Acknowledgments

This work would not have been possible without the contributions by T Albaret, B Amadon, F Bottin, P Casek, L Giordano, C Mottet, A Pojani, and W Vervisch.

References

[1] Henrich V E and Cox P A 1994 *The Surface Science of Metal Oxides* (Cambridge: Cambridge University Press)
[2] Noguera C 1996 *Physics and Chemistry at Oxide Surfaces* (Cambridge: Cambridge University Press)
[3] Onishi H and Iwasawa Y 1996 *Phys. Rev. Lett.* **76** 791
[4] Surnev S, Kresse G, Ramsey M G and Netzer F P 2001 *Phys. Rev. Lett.* **87** 086102
[5] Barbier A, Mocuta C and Renaud G 2000 *Phys. Rev.* B **62** 16056
[6] Dulub O, Diebold U and Kresse G 2003 *Phys. Rev. Lett.* **90** 016102
[7] Kuhlenbeck H and Freund H J 1997 *Growth and Properties of Ultrathin Epitaxial Layers (The Chemical Physics of Solid Surfaces)* vol 8, ed D A King and D P Woodruff (Amsterdam: Elsevier)

[8] Noguera C 2001 *The Chemical Physics of Solid Surfaces (Oxide Surfaces)* vol 9, ed P Woodruff (Amsterdam: Elsevier) p 35
[9] Heiz U and Schneider W D 2000 *J. Phys. D: Appl. Phys.* **33** R85
[10] Finocchi F and Noguera C 2000 *Acid–Base Interactions* vol 2, ed K Mittal (Utrecht: VSP) pp 187–204
[11] Noguera C, Pojani A, Casek P and Finocchi F 2002 *Surf. Sci.* **507–510** 245
[12] Shaikhutdinov S K, Joseph Y, Kuhrs C, Ranke W and Weiss W 1999 *Faraday Discuss.* **114** 363
[13] Hohenberg P and Kohn W 1964 *Phys. Rev.* B **136** 864
[14] Kohn W and Sham L J 1965 *Phys. Rev.* A **140** 1133
[15] Noguera C 2001 *Surf. Rev. Lett.* **8** 121–67
[16] Tung R T 2001 *Mater. Sci. Eng.* R **35** 1
Tung R T 2001 *Phys. Rev.* B **64** 205310
[17] Tersoff J 1984 *Phys. Rev. Lett.* **52** 465
[18] Bordier G and Noguera C 1991 *Phys. Rev.* B **44** 6361
[19] Goniakowski J and Noguera C 2003 *Interface Sci.* at press
[20] Goniakowski J 1998 *Phys. Rev.* B **57** 1935
[21] Goniakowski J 1999 *Phys. Rev.* B **59** 11047
[22] Nowotny J and Weppner W 1989 *Non-Stoichiometric Compounds: Surfaces, Grain Boundaries and Structural Defects* (*NATO ASI Series C* vol 276) (Dordrecht: Kluwer–Academic)
[23] Noguera C, Pojani A, Finocchi F and Goniakowski J 1997 *Chemisorption and Reactivity on Supported Clusters and Thin Films* (*NATO ASI Series E: Applied Sciences* vol 331) ed R M Lambert and G Pacchioni (Dordrecht: Kluwer–Academic)
[24] Castanier E and Noguera C 1996 *Surf. Sci.* **364** 17
[25] Finocchi F, Goniakowski J and Noguera C 1999 *Phys. Rev.* B **59** 5178
[26] Langel W and Parrinello M 1995 *J. Chem. Phys.* **103** 324
[27] Giordano L, Goniakowski J and Suzanne J 1998 *Phys. Rev. Lett.* **81** 1271
[28] Odelius M 1999 *Phys. Rev. Lett.* **82** 3919
[29] Finocchi F and Goniakowski J 2001 *Phys. Rev.* B **64** 125426
[30] Ahmed S I, Perry S S and El-Bjeirami O 2000 *J. Phys. Chem.* B **104** 3343
[31] Gail H P and Sedlmayr E 1998 *Faraday Discuss.* **109** 303
[32] Albaret T, Finocchi F and Noguera C 1999 *Faraday Discuss.* **114** 285
[33] Albaret T, Finocchi F and Noguera C 2000 *J. Chem. Phys.* **113** 2238
[34] Noguera C and Mackrodt W C 2000 *J. Phys.: Condens. Matter* **12** 2163
[35] Janak J F 1978 *Phys. Rev.* B **18** 7165
[36] Parr R G and Yang W 1989 *Density Functional Theory of Atoms and Molecules* (Oxford: Oxford University Press)
[37] Chermette H 1999 *J. Comput. Chem.* **20** 129
[38] Garcia A and Cohen M L 1993 *Phys. Rev.* B **47** 4215
[39] Bader R F W 1990 *Atoms in Molecules: a Quantum Theory* (Oxford: Oxford University Press)
[40] Bader R F W 1991 *Chem. Rev.* **91** 893
[41] Sousa C, Illas F, Bo C and Poblet J M 1993 *Chem. Phys. Lett.* **215** 97
[42] Böttger H 1983 *Principles of the Theory of Lattice Dynamics* (Weinham: Physik-Verlag)
[43] Vidal-Valat G, Vidal J P and Kurki-Suonio K 1978 *Acta Crystallogr.* A **34** 594
[44] Sasaki S, Fujino K, Takéuchi Y and Sadanaga R 1980 *Acta Crystallogr.* A **36** 904
[45] Kuntzinger S, Ghermani N E, Dusausoy Y and Lecomte C 1998 *Acta Crystallogr.* B **54** 819
[46] Gonze X *et al* 2002 *Comput. Mater. Sci.* **25** 478 and see also http://www.abinit.org
[47] Noguera C 2000 *J. Phys.: Condens. Matter* **12** R367
[48] Pojani A, Finocchi F, Goniakowski J and Noguera C 1997 *Surf. Sci.* **387** 354
[49] Finocchi F, Jupille J, Barbier A and Noguera C 2003 in preparation
[50] White I D, Godby R W, Rieger M and Needs R J 1998 *Phys. Rev. Lett.* **80** 4265
[51] Pulci O, Bechstedt F, Onida G, Del Sole R and Reining L 1999 *Phys. Rev.* B **60** 16758
[52] Svane A and Gunnarsson O 1990 *Phys. Rev. Lett.* **65** 1148
[53] Dudarev S L, Peng L-M, Savrasov S Y and Zuo J-M 2000 *Phys. Rev.* B **61** 2506
[54] Kodderitzsch D, Hergert W, Temmerman W M, Szotek Z, Ernst A and Winter H 2002 *Phys. Rev.* B **66** 064434
[55] Amadon B, Finocchi F and Noguera C 2002 *J. Phys.: Condens. Matter* **14** 4699
[56] Bechstedt F, Del Sole R, Cappellini G and Reining L 1992 *Solid State Commun.* **84** 765
[57] Albaret T, Finocchi F, Noguera C and de Vita A 2002 *Phys. Rev.* B **65** 035402
[58] Wang X G, Weiss W, Shaikhutdinov S K, Ritter M, Petersen M, Wagner F, Schlögel R and Scheffler M 1998 *Phys. Rev. Lett.* **81** 1038

[59] Batyrev I G, Alavi A and Finnis M W 2000 *Phys. Rev.* B **62** 4698
[60] Reuter K and Scheffler M 2001 *Phys. Rev.* B **65** 035406
[61] Pojani A, Finocchi F and Noguera C 1999 *Surf. Sci.* **442** 179
[62] Bottin F, Finocchi F and Noguera C 2003 *Phys. Rev.* B at press
[63] Wander A, Schedin F, Steadman P, Norris A, McGrath R, Turner T S, Thornton G and Harrison N M 2001 *Phys. Rev. Lett.* **86** 3811
[64] Car R and Parrinello M 1985 *Phys. Rev. Lett.* **55** 2471
[65] Johnson M A, Stefanovich E V, Truong T N, Gunster J and Goodman D W 1999 *J. Phys. Chem.* B **103** 3391
[66] Cho J H, Park J M and Kim K S 2000 *Phys. Rev.* B **62** 9981
[67] Delle Site L, Alavi A and Lynden-Bell R M 2000 *J. Chem. Phys.* **113** 3344
[68] Ferry D, Glebov A, Senz V, Suzanne J, Toennies J P and Weiss H 1996 *J. Chem. Phys.* **105** 1697
[69] Giordano L, Goniakowski J and Suzanne J 2000 *Phys. Rev.* B **62** 15406
[70] Yamamoto K, Kasukabe Y, Takeishi R and Osaka T 1996 *J. Vac. Sci. Technol.* A **14** 327
[71] Yamauchi R, Kubo M, Miyamoto A, Vetrivel R and Broclawik E 1998 *J. Phys. Chem.* B **102** 795
[72] Benedek R, Alavi A, Seidman D N, Yang L H, Muller D A and Woodward C 2000 *Phys. Rev. Lett.* **84** 3362
[73] Oviedo J, Fernández Sanz J, López N and Illas F 2000 *J. Phys. Chem.* B **4** 4342
[74] Vervisch W, Mottet C and Goniakowski J 2002 *Phys. Rev.* B **65** 245411
[75] Rosato V, Guillopé M and Legrand B 1984 *Phil. Mag.* A **59** 321
[76] Goniakowski J 1998 *Phys. Rev.* B **58** 1189
[77] Giordano L, Goniakowski J and Pacchioni G 2001 *Phys. Rev.* B **64** 075417